Article

Significantly accelerated photochemical and photocatalytic reactions in microdroplets

Kejian Li, Kedong Gong, Juan Liu, ..., Minbiao Ji, Ventsislav K. Valev, Liwu Zhang

zhanglw@fudan.edu.cn

Highlights

Photochemistry and photocatalysis are studied in microdroplets of varying diameters

Organic degradation exponentially increases with decreasing the microdroplet size

O_2 availability is improved in microdroplets

pH alteration and species interfacial enrichment are observed via SRS chemical imaging

Li et al. study photochemistry and photocatalysis in microdroplets using micro-Raman spectrometry. The photooxidation of organic compounds exponentially increases with decreasing microdroplet diameter, which is attributed to the special air-water interface properties of the microdroplets, including O_2 accessibility enhancement, pH alteration, and species interfacial enrichment.

Article

Significantly accelerated photochemical and photocatalytic reactions in microdroplets

Kejian Li,[1,2,7] Kedong Gong,[1,7] Juan Liu,[1] Lukas Ohnoutek,[3,4,5] Jianpeng Ao,[6] Yangyang Liu,[1] Xi Chen,[1] Guanjun Xu,[1] Xuejun Ruan,[1] Hanyun Cheng,[1] Jin Han,[1] Guodong Sui,[1,2] Minbiao Ji,[6] Ventsislav K. Valev,[3,4,5] and Liwu Zhang[1,2,8,*]

SUMMARY

Photochemistry and photocatalysis are promising approaches to derive solar energy for solving the global energy and environment crisis. However, some practical aspects remain daunting, mainly due to the slow reaction kinetics, especially for multiphase reactions involving gaseous reactants. Here, we report that the oxidation of methyl orange, golden orange II, and levoglucosan by Fe(III)-oxalate photochemistry and by g-C_3N_4 photocatalysis can be significantly increased (up to two orders of magnitude) with decreasing microdroplet diameter, from around 2,000 to 100 μm. Using simulated Raman scattering microscopy, we observe strong interface enrichment and pH alternation within the microdroplets. Experimental and theoretical results indicate that the rate increase is mainly caused by the size-dependent air-water interface properties of microdroplets. Furthermore, we demonstrate the scalability of microdroplet photoreactions. This work not only provides an efficient pathway for improving the photochemistry and photocatalysis efficiencies but also shows important implications for atmospheric photochemistry.

INTRODUCTION

Photochemistry and photocatalysis are of great potential for converting solar energy into chemical energy and for environmental contaminant decomposition.[1,2] To date, great efforts have been invested to improve solar energy conversion efficiency, but those were mainly focusing on materials engineering (e.g., semiconductor heterojunctions) and photoreactor design (e.g., microfluidic reactor).[3,4] However, sluggish reaction kinetics largely impede the practical applications. Molecular oxygen is a natural electron acceptor, and O_2 activation by photochemistry and photocatalysis is an efficient approach for the formation of reactive oxygen species (ROS).[5,6] Unfortunately, because traditional aqueous O_2 photoactivation is generally performed in bulk solution at room temperature and pressure, the low solubility and slow diffusivity of O_2 limit its concentration at the active sites and, in effect, the subsequent reaction processes.[3,7] Therefore, a promising approach would be to increase the availability of O_2 to the reaction system in order to promote the photoreaction rate.

One efficient strategy to promote catalytic reaction is using nanocatalysts rather than bulk material, which are of abundant active sites and have been widely studied in solid catalysts.[8,9] Similarly, dividing bulk aqueous solution into micro- or even nanosized liquids ("nano liquid") can increase the surface-area-to-volume ratio (S/V) by several orders of magnitude compared with the bulk solution.[10] Recently, microdroplets, generated in

[1]Shanghai Key Laboratory of Atmospheric Particle Pollution and Prevention, Department of Environmental Science and Engineering, Fudan University, Shanghai 200433, People's Republic of China

[2]Shanghai Institute of Pollution Control and Ecological Security, Shanghai 200092, People's Republic of China

[3]Centre for Photonics and Photonic Materials, University of Bath, Bath BA2 7AY, UK

[4]Centre for Nanoscience and Nanotechnology, University of Bath, Bath BA2 7AY, UK

[5]Centre for Therapeutic Innovation, University of Bath, Bath BA2 7AY, UK

[6]State Key Laboratory of Surface Physics and Department of Physics, Fudan University, Shanghai 200433, People's Republic of China

[7]These authors contributed equally

[8]Lead contact

*Correspondence: zhanglw@fudan.edu.cn
https://doi.org/10.1016/j.xcrp.2022.100917

the course of electrospray-based ionization, are of increasing interest for chemical-reaction acceleration compared with the bulk-phase counterpart.[11] It has been extensively reported that organic additions and condensation,[12–14] SO_2 oxidation,[15–17] Fenton chemistry,[18] and the reactions of amines with CO_2[19] can be dramatically accelerated in microdroplets. Besides, the alcohol oxidation in microdroplets under light and thermal irradiation was also accelerated.[20] Moreover, the microdroplets can induce a spontaneous reduction of organics and $HAuCl_4$,[21,22] H_2O_2 production,[23] and ribonucleotide synthesis[24] in the absence of any reducing agent. At present, the intriguing behaviors in microdroplets are arguably attributed to the different reaction environments between microdroplets and bulk solution, especially at the air-water interface, including effective mass transfer and mixing, pH alteration, surface partial solvation, ordered molecular orientation, interfacial enrichment, and interfacial electric field.[25–27] Photo-Fenton and semiconductor photocatalysis are promising technologies for organic decomposition.[28,29] However, the multiphase photochemistry and photocatalysis in microdroplets have rarely been explored,[30] and the microdroplet size effect on the photoreaction is still not well known. With the above considerations in mind, we hypothesize that the large S/V and the special air-water-interfacial properties of microdroplets can increase gaseous reactants availability, and that, in addition, they offer other advantages for accelerating the photochemical and photocatalytic reactions.

Herein, we perform homogeneous and heterogeneous photoreactions in microdroplets to show the concept of nano-liquid catalysis. To clarify, here, homogeneous photochemistry means that the photoactive species can dissolve into water, while the heterogeneous photocatalysis means that solid nanocatalysts are uniformly dispersed in solution. Fe(III)-oxalate photochemistry and g-C_3N_4 photocatalysis are used as model systems because the reduction of oxygen is a critical step for ROS formation in the two cases. Using micro-Raman spectroscopy, we find that organic degradation is significantly accelerated in microdroplets (up to two orders of magnitude) compared to the bulk phase. This dramatic photoreaction acceleration is predominantly attributed to the special size-dependent air-water interface properties of microdroplets (e.g., O_2 availability improvement and species enrichment). Furthermore, opening the way to potential large-scale applications, the scalability of microdroplet photoreactions is demonstrated.

RESULTS AND DISCUSSION

Photochemical organic oxidation in microdroplets

Figure 1A shows a schematic illustration of the setup for studying microdroplet photochemistry and photocatalysis. The microdroplets were generated on a superhydrophobic substrate (water contact angle [CA], 148 ± 2°, inset in Figure 1B) via spraying the as-prepared bulk solution using a nebulizer. A confocal micro-Raman spectrometer coupled with a ×10 Olympus microscope objective was used to monitor the microdroplet size and organic concentration during the microdroplet photoreaction (see details in supplemental experimental procedures). As shown in Figure S1, the microdroplet diameters were in the range of 100–1,000 μm. The wide distribution of microdroplet size is conducive to investigate the microdroplet size effects on photoreactions. Meanwhile, the microdroplet generation method is of great repeatability, favoring independent repeated experiments. Notably, the reported degradation rates are the average value obtained from at least five independent microdroplets with similar size (standard deviation, <2%).

Firstly, we investigated the methyl orange (MO) photodegradation by Fe(III)-oxalate photochemistry in microdroplets of different sizes. Fe(III)-oxalate complexes,
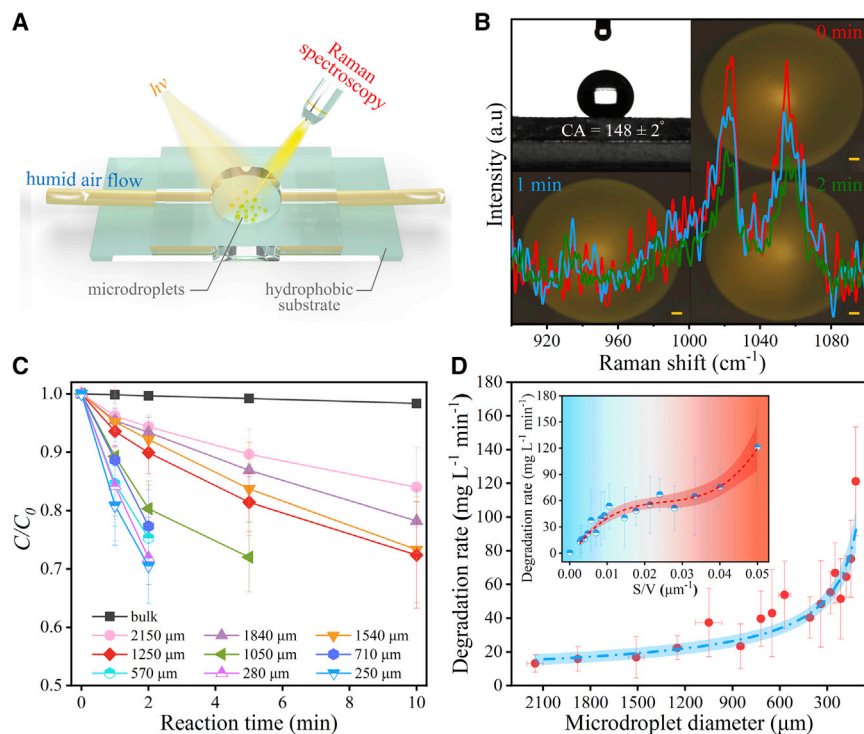
Figure 1. MO degradation performances in microdroplets by Fe(III)-oxalate photochemistry

(A) Schematic illustration of the experimental setup.

(B) Raman spectra of MO in a microdroplet and micrographs of the microdroplet measured at the specific time interval (scale bar: 20 μm). The inset in the top left is photograph of a water droplet on an as-prepared superhydrophobic substrate.

(C) C/C_0 of MO in bulk phase and microdroplet as a function of irradiation time, where C_0 and C are the concentrations of MO at beginning and sampling time t, respectively.

(D) MO photooxidation rates and fitting curves in microdroplets of different sizes. The error bars represent the standard deviation determined by at least five independent experiments. Unless otherwise stated, the experimental conditions were $FeCl_3$, 1 mM; $Na_2C_2O_4$, 7 mM; MO, 350 mg L^{-1}; initial pH, 4.75; Xe lamp irradiation, ~35.7 mW cm^{-2}.

widespread composites in natural environments, are photochemically active to produce a series of ROS (shown in Table S1).[31] Figures 1B and S2 show representative micrographs of a microdroplet and corresponding organics' Raman spectra sampled at the pre-designed irradiation time (here, the irradiation time refers to the reaction time). It clearly shows that the organic concentration (proportional to the Raman peaks intensity) decreased with the time increasing, while the diameter of the microdroplet changed insignificantly due to our low-temperature and high-humidity control (less than 10%). Figure 1C shows that the MO photodegradation rate (5 min irradiation) in 2 mL bulk phase was only 0.54 mg L^{-1} min^{-1}. Interestingly, the photodegradation rates in microdroplet with initial diameters (Φ) of about 2,150, 1840, 1,540, 1,250, and 1,050 μm were approximatluy 7.2, 9.2, 11.4, 13.1, and 19.6 mg L^{-1} min^{-1}, respectively. The pseudo first-order reaction kinetics model fitting (Figure S3) indicated the MO photooxidation rate constant in a ~1,050 μm diameter microdroplet was approximately 46.6-fold higher than that of a traditional liquid-phase system. The results explicitly confirm that the photooxidation performance of Fe(III)-oxalate complexes is dramatically increased in microdroplets. Figure 1D indicated that the MO degradation rates were exponentially increased as the microdroplets diameter decreased from about 2,000 to 100 μm (especially for Φ < 300 μm), and it reached about 121.2 mg L^{-1} min^{-1} in a 120 μm diameter

**Cell Reports
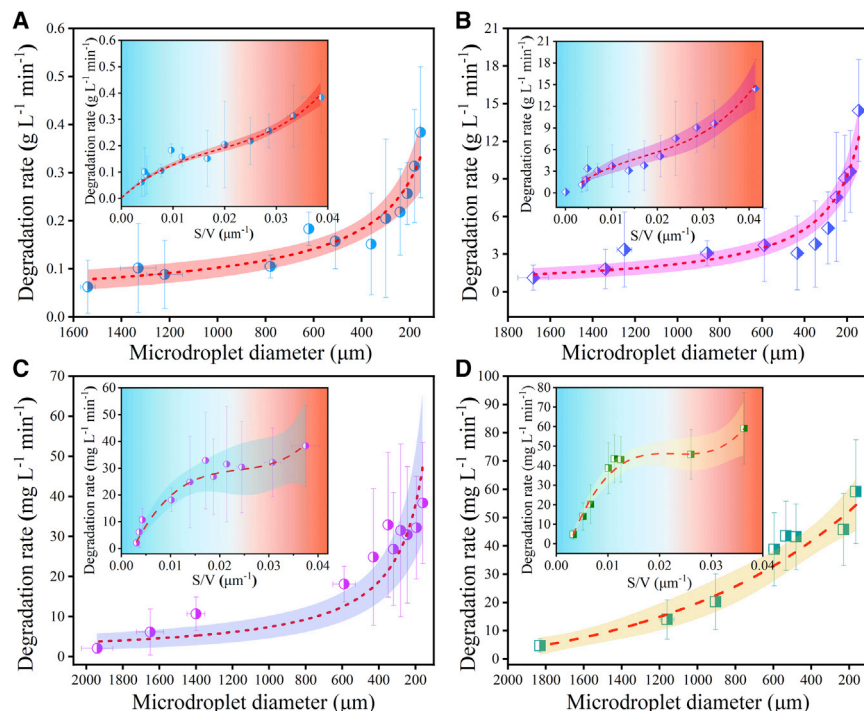Physical Science**
Article

Figure 2. Universality of photoreactions acceleration in microdroplets

(A and B) GO and LV degradation by Fe(III)-oxalate photochemistry. Conditions: $FeCl_3$, 1 mM; $Na_2C_2O_4$, 7 mM; GO, 1.5 g L^{-1}; LV, 50 g L^{-1}; initial pH, 4.75; Xe lamp irradiation, $\sim$35.7 mW cm^{-2}.

(C and D) Photocatalytic MO and GO degradation in microdroplets. Conditions: g-C_3N_4 dosage, 0.1 g L^{-1}; MO, 350 mg L^{-1}; GO, 1.5 g L^{-1}; 365 nm UV lamp illumination, $\sim$5.6 mW cm^{-2}. The insets are the fitted relations between degradation rate and microdroplet S/V. The error bars represent the standard deviation of at least five repeats.

microdroplet, which is approximately 215-fold higher than that of the bulk-phase reaction (0.56 mg L^{-1} min^{-1}). The variation trend of MO photodegradation rates relative to the microdroplet diameter is similar to most of the previous microdroplet chemistry studies.[23,24] The photodegradation rates versus microdroplet S/V is depicted in the inset of Figure 1D. In addition, the changes of organic oxidation rates (defined as $\Delta R/(\Delta S/V)$, where R is the organic degradation rates) as a function of the microdroplet S/V are shown in Figure S4. Two regions with an inflection point at S/V of around 0.025 μm^{-1} could be clearly observed, which means that the $\Delta R/(\Delta S/V)$ was firstly decreased and then increased with decreasing the microdroplet diameter. The potential reasons will be discussed later.

To confirm the significantly improved oxidation performances of Fe(III)-oxalate in microdroplets, the degradation of golden orange II (GO) and levoglucosan (LV) was studied; the former is another example of organic dye,[32] and the latter is a typical organic molecule in atmosphere.[33] As displayed in Figures 2A and 2B, the photodegradation rates of GO and LV were about 0.36 and 14.45 g L^{-1} min^{-1} in microdroplets with Φ of $\sim$155 and $\sim$145 μm, respectively, which are at least two orders of magnitude higher than that of bulk phase (only about 0.003 and 0.12 g L^{-1} min^{-1}, respectively; Figure S5). The photodegradation rates of the two organics were also exponentially increased with decreasing the microdroplet diameter, and the fitted relations between degradation rate and S/V (Figures 2A and 2B, insets) showed a close resemblance to that observed during MO photodegradation.

CellPress
OPEN ACCESS

Heterogeneous photocatalysis in microdroplets

We studied MO and GO degradation by g-C_3N_4 photocatalysis in microdroplets as another model system. The photocatalytic degradation of MO and GO was significantly accelerated in microdroplets compared with the bulk-phase counterpart. For example, the MO removal efficiency and rate constant in a ~1,400 μm diameter microdroplet were about 25-times and 93-fold greater than that of bulk phase (6.8 versus 0.27 mg L^{-1} min^{-1}, 0.0186 versus 0.0002 min^{-1}, 10 min irradiation; Figure S6). At present, GO and LV degradation under a longer reaction time course is not shown, but all reactions follow pseudo first-order reaction kinetics. In addition, the organic photocatalytic degradation (Figures 2C and 2D) was strikingly increased as the microdroplet diameter decreased. The degradation rates in microdroplets with diameters of about 160 μm were accelerated by about 135 and 102 times for MO and GO compared with the bulk solution (38.3 versus 0.29 mg L^{-1} min^{-1}; 59.2 versus 0.58 mg L^{-1} min^{-1}), respectively. Moreover, the fitting curves of MO and GO photocatalytic degradation rates versus microdroplet S/V were similar with that observed in the Fe(III)-oxalate microdroplet photochemistry system. Unfortunately, the error bars are large in the microdroplets system. Generally, the Raman spectroscopy measurements are sensitive to ambient environmental conditions including relative humidity and temperature. In addition, despite our best efforts, the water evaporation of microdroplets does vary between independent repeated experiments. Thus, the error bars show the effects of environmental conditions and water evaporation. Meanwhile, the negligible photodegradation of MO without any of the essential components (light irradiation, photoactive species, and O_2) indicated that the significant benefit of microdroplet for photoreaction acceleration are reliable.

Improved oxygen availability

Firstly, the predominant ROS responsible for MO photodegradation in the Fe(III)-oxalate microdroplet system were investigated through radical quenching experiments with p-benzoquinone (p-BQ; 10 mM) as the O_2^- quencher and tertiary butanol (TBA; 30 mM) as the ·OH scavenger. As shown in Figure 3A, the addition of p-BQ almost completely inhibited MO photodegradation in microdroplets, while the presence of TBA insignificantly influenced MO photodegradation, implying that O_2^-, produced from O_2 reduction, played a critical role in organic oxidation.[34,35] The MO photocatalytic and photochemical degradations in microdroplets under N_2 atmosphere were also significantly suppressed compared with the air environment (Figures S7 and S8). Therefore, O_2 availability is important for the O_2^- production and photooxidation in the two systems.

Under a sealed N_2 environment, we observed that as the reaction proceeded, there was hardly any further degradation of MO in microdroplets due to the depletion of the remaining oxygen in the atmosphere (Figure 3B). When the microdroplet was exposed to air, the degradation was evidently increased from 14.9% to 40.9% in 10 min. However, in the bulk phase, the exposure to air from N_2 atmosphere increased the MO photodegradation only slightly (from 2.1% to 3.8%). Meanwhile, in the bulk phase, the concentration of dissolved oxygen (DO) during the photochemical reaction rapidly decreased from ~8 to ~0 mg L^{-1} in less than 20 min (Figure 3C), and the increase of DO was very slow (from ~0 to ~0.4 mg L^{-1} after 30 min) under dark conditions. Unfortunately, due to experimental limitations of the DO measurement meter (Figure S9), it was not possible to directly observe the changes of DO concentrations in microdroplets as the reaction proceeded. It is, however, well known that the oxygen diffusion coefficient in the air phase (2.0×10^{-1} cm^2 s^{-1}) is four orders of magnitude higher than that in the water phase (2.1×10^{-5} cm^2 s^{-1}).[36] Thus, for bulk-phase photoreaction, the electron acceptor oxygen
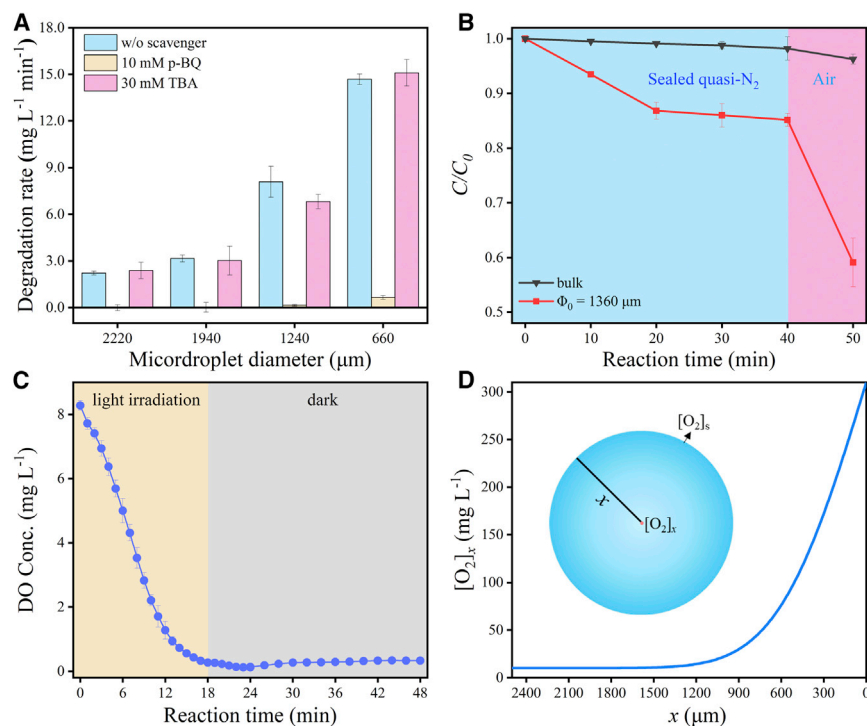
Figure 3. The role of O_2 availability on photoreactions acceleration

(A) MO photodegradation rates in microdroplets with radical quenchers.

(B) MO photodegradation performances in microdroplets and bulk phase under different reaction atmospheres.

(C) Changes of DO concentration during Fe(III)-oxalate photoreaction in bulk solution.

(D) Simulated oxygen concentration at the center of microdroplets using Fick's second law. The error bars represent the standard deviation of at least three repeats.

is mainly situated at the air-liquid interface, and it is difficult for it to transfer into the internal region due to the long diffusion distance, leading to the rapid depletion of DO and slow reaction kinetics. Unequivocally, the microdroplets with confined volume and shortened diffusion distance can obtain oxygen directly and efficiently from air, facilitating ROS formation and organic oxidation.

A theoretical study of the oxygen-concentration distribution in microdroplets was then performed. Because the oxygen concentration is varied as the photoreaction proceeds, a typical case of Fick's second law (Equation 1) was employed to qualitatively analyze the oxygen-concentration distribution in the reaction system.

$$\frac{[O_2]_s-[O_2]_x}{[O_2]_s-[O_2]_0} = erf\left(\frac{x}{2\sqrt{Dt}}\right), \qquad \text{(Equation 1)}$$

where $[O_2]_s$, $[O_2]_x$, and $[O_2]_0$, respectively, represent the O_2 concentration at the air-liquid interface (regarded as O_2 concentration in the air, 310 mg L^{-1}),[37] the O_2 concentration at the distance x from the air-water interface (for a microdroplet, it is the oxygen concentration at the center), and the initial oxygen concentration in the solution (8 mg L^{-1});[38] D is the oxygen diffusion coefficient in water (2.1×10^{-5} cm^2 s^{-1}); and t is the reaction time. As displayed in Figure 3D, $[O_2]_x$ will be significantly higher with decreasing x (t = 60 s), implying that smaller microdroplets can provide more efficient oxygen availability. In order to visualize the enhanced O_2 accessibility in microdroplets, the color change of alkaline phenolphthalein was observed in the presence of high-concentration CO_2. As displayed in Video S1 (color variance of alkaline
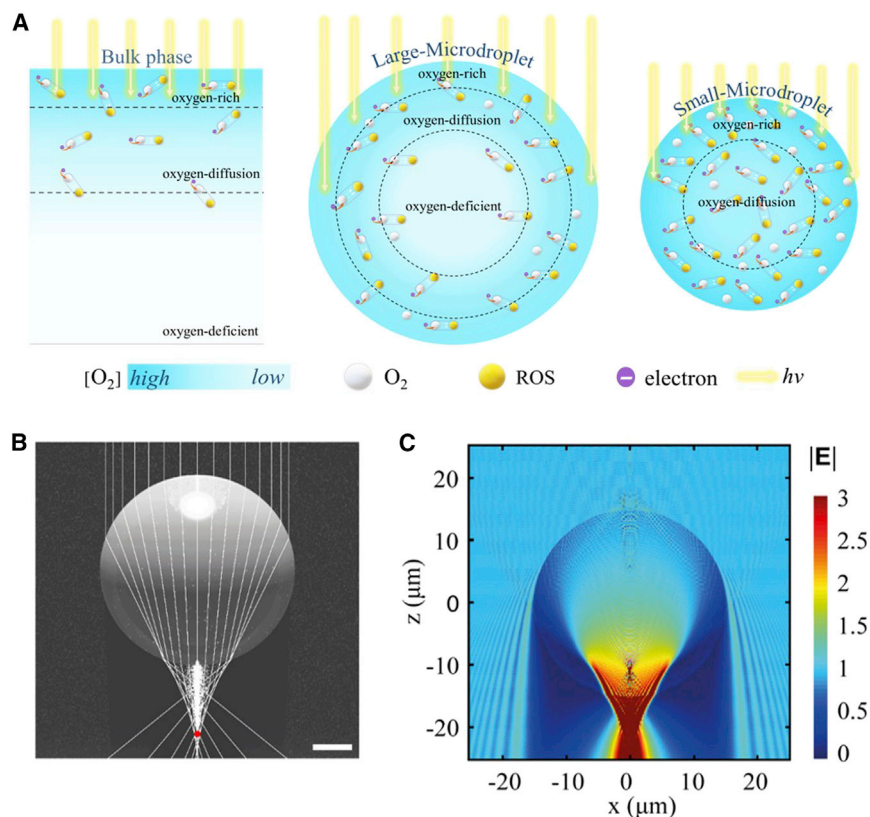
CellPress
OPEN ACCESS

Figure 4. O₂ concentration and optical-field distribution in microdroplets

(A) The inhomogeneous O_2 concentration distribution in bulk solution, and large microdroplets and small microdroplets during photoreaction.

(B) Geometric optics results. In the background, ray-tracing software simulation of light incident on a sphere with refractive index of water. The scale bar corresponds to 5 a.u. of length. The red dot corresponds to the calculated point of effective focal length. The white lines are light rays calculated by Snell's law.

(C) Electromagnetic-wave results. Finite-difference time-domain simulation of the electromagnetic field amplitudes of a 30 μm (diameter) water microdroplet illuminated at 400 nm.

phenolphthalein in microdroplets), the pink in microdroplets of varying size rapidly disappeared, and the time required for color fading was shorter in smaller microdroplets. The color disappearance was caused by solution acidification due to the reaction between CO_2 and OH^- and the CO_2 dissolution. By contrast, the color of bulk solution negligibly changed even after 1 h (Figure S10). Moreover, it was observed that the pink in big droplets slowly disappeared from the external surface to the interior region, probably due to the comparatively large volume and slow reagents diffusion.[25] Thus, we propose that, for bulk solution and microdroplet of large size, the system can be divided into three regions based on the availability of O_2 during photoreaction: (1) interfacial O_2-rich region, (2) O_2-diffusion region, and (3) O_2-deficient region, as illustrated in Figure 4A. In bulk solution and large-sized microdroplets, the third region is dominant during photoreaction, leading to inefficient O_2 activation and ROS production. As the size of the microdroplet decreases, the third region becomes smaller and eventually disappears.

Optical-field distribution

In microdroplets, the spherical geometry determines the regions of light-matter interaction. As Figure 4 illustrates, the light distribution inside the microdroplets

is not homogeneous. For big droplets, large parts of the oxygen-rich and oxygen-diffusion regions experience low levels of illumination, whereas the oxygen-deficient regions are well illuminated. Consequently, for big droplets, the photoreactions are less efficient than in the case of small microdroplets, whose core does contain oxygen during photoreaction. Furthermore, to illustrate the illumination within very big and very small microdroplets, we conducted both geometric optical (Figure 4B) and electromagnetic wave simulations (Figure 4C). Figure 4B shows a ray-tracing simulation of a sphere with the refractive index (n) of water (n = 1.339). The red dot corresponds to the effective focal length that depends on n and on the diameter of the sphere. The white lines are individual rays calculated by Snell's law. Clearly, large parts of the surface regions are "in the shadow." The simulations in Figure 4B are valid for any droplet size, for which the conditions of geometrical optics remain valid; this is why the scale bar is provided in arbitrary units. Naturally, with decreasing droplet size, geometrical optics fails. We therefore need to establish a reasonable lower limit of validity. Figure 4C corresponds to a finite-difference time-domain simulation of a water microdroplet with a diameter of 30 μm, illuminated at 400 nm. This figure shows the electromagnetic (EM) field distribution within the microdroplet. The results are normalized to the incident EM field. The regions in dark blue correspond to low light (EM fields <1), and they cover almost the entire surface region. A comparison between Figures 4B and 4C shows that the light profiles are very similar. It follows that the geometric optics simulation in Figure 4B is valid down to water microdroplets with a diameter of 30 μm. Therefore, it is certainly valid for larger droplets, such as those in the range of this study (from 100 to 2,000 μm).

Interfacial enrichment and pH alteration

Although the improved O_2 availability and light absorption can accelerate the photoreaction, the two factors cannot completely explain the appearance of an inflection point in the relation curves of organics photodegradation rates versus microdroplet S/V. Thus, there are additional reasons behind the photoreaction acceleration, especially for smaller microdroplets. The pH changes in microdroplets compared with bulk solution were qualitatively investigated via Raman spectroscopy. As shown in Figure S11, in bulk solution, a red shift of a Raman peak attributed to C–C bond (v(C–C)) of oxalate is found with decreasing solution pH (adjusted using NaOH and HCl), probably owing to the protonation effects.[39] Intriguingly, the red shift of v(C–C) is also clearly observed between big microdroplet and small microdroplet via simulated Raman scattering (SRS) microscopy (Figure 5A), implying that the smaller microdroplet presents a lower pH value.[40,41] The bulk-phase experiments displayed that MO photooxidation by Fe(III)-oxalate photochemistry is faster under more acidic condition (Figure S12A).[42] Previous microdroplet chemistry studies also opined that the pH alteration in microdroplets relative to bulk solution is favorable to the acid/base catalyzed reactions, based on the results of traditional bulk-phase reaction.[27,43] Thus, the more acidic environment of smaller microdroplets might be favorable for ROS formation and photooxidation.

Additionally, near and at the air-water interface of microdroplets, the "water-poor" character, disruption of the hydrogen-bonding network, and ordered molecular orientation could influence the solvation effects, induce species enrichment, and alter the thermodynamics and kinetics of redox reactions.[44,45] Here, SRS was conducted to explore the concentration enrichment of Fe(III)-oxalate at the air-water interface. The spatial distribution of Raman spectra assigned to v(C–C) and v(O–H) in a microdroplet (Φ = 55 μm) was shown in Figures 5B and 5C, respectively, where v(O–H) is attributed to the O–H bond of water molecules. The SRS intensity of v(O–H)
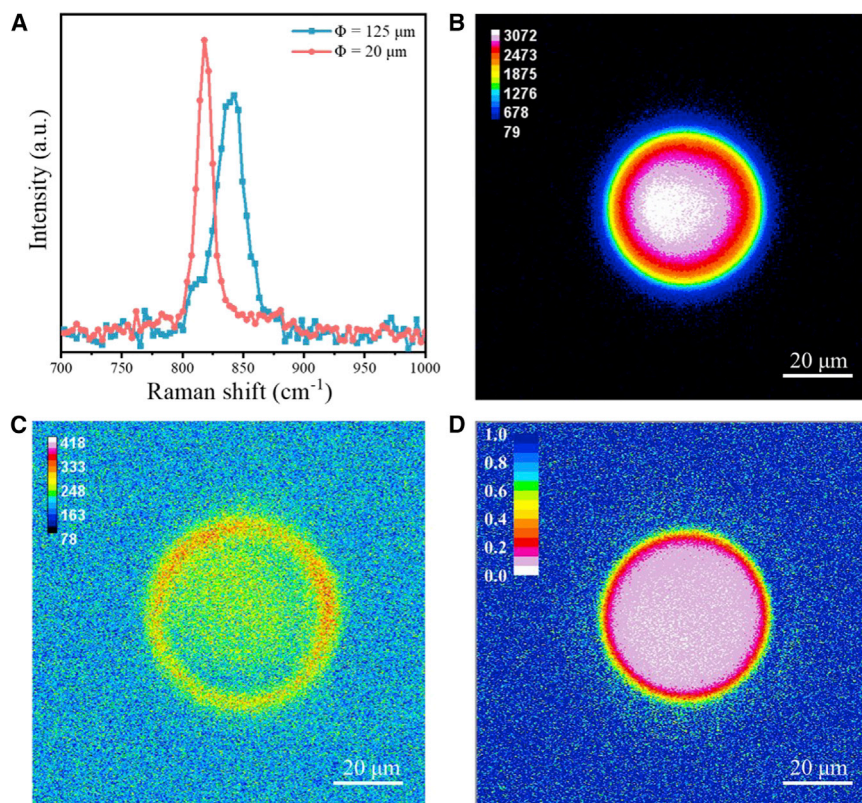
CellPress
OPEN ACCESS

Figure 5. pH alternation and interfacial enrichment in microdroplets
(A) SRS spectra of v(C–C) in microdroplets of different sizes.
(B and C) The distribution of SRS spectra of v(O–H) and v(C–C) in a microdroplet, respectively.
(D) SRS intensity ratio of v(C–C) to v(O–H) in a microdroplet.

gradually decrease from the center to the edge because the number of detected molecules decreased at the droplet edge,[27] while an abnormally high SRS intensity of v(C–C) at the surface region was observed, implying a possible species enrichment at the surface region. According to internal standard methods,[46] the peak intensity ratio of v(C–C) to v(O–H) can be an indicator of species concentration. As presented in Figure 5D, it is clear that the ratio of v(C–C) to v(O–H) near the surface region of a microdroplet (thickness of 5 ~μm) is about 5-fold higher than that in the interior region, implying an enrichment of oxalate at the air-water interface.[47–49] As previously reported, the Fe(III) species are also more abundant at the water surface.[50] Owing to the very strong complexation affinity between Fe^{3+} and $C_2O_4^{2-}$, the Fe(III)-oxalate chelates would be concentrated near the interfacial region, which is beneficial to the organic photooxidation (Figure S12B).[49] Furthermore, the molecular-dynamics simulations indicated that, at the air-water interface, the redox potential of $O_2/O_2^{\bullet-}$ couple can decrease -0.32 V, which is as large as the experimental value of -0.33 V, making the oxygen reduction by $CO_2^{\bullet-}$ radical and photogenerated electrons easier.[51] Thus, it is reasonable to suggest that the unique properties of the air-water interface are beneficial to the microdroplet photoreactions.

As abovementioned, the inflection points were clearly observed in Figure S4 and the insets in Figures 1 and 2. On the one hand, the contributions of O_2 accessibility on reaction acceleration would reach a stable state in small microdroplets, due

to the almost same O_2 transfer capacity. On the other hand, the roles of unique air-water-interface characteristics of microdroplets would be strengthened and the proportion of interfacial region in a microdroplet will increase with decreasing the microdroplets diameter.[52] With the above considerations, we speculate that the varied contribution ratios of O_2 availability and air-water interfacial properties synergistically led to the observed inflection points.

The faster photoreaction near the air-water interface of the bulk solution or a large microdroplet is further confirmed by observing the formation of γ-FeOOH in the Fe(III)-oxalate photochemistry system. As shown Table S1 and Figure S13, the pH value will increase during the photochemical reaction, resulting in a formation of γ-FeOOH nanosheets as confirmed by X-ray diffraction pattern, Raman spectra, and transmission electron microscopy (Figure S14).[53,54] It was observed that the γ-FeOOH was merely formed at the gas-liquid interface in bulk solution after ~80 min (Figure S15A). In a large droplet with Φ of ~1,570 μm, the γ-FeOOH was first dominantly produced at the external surface region (appeared after about 4 min; Figure S15B) and then gradually appeared in the deeper interior as the photoreaction proceeded (Figure S16). Interestingly, in a ~315 μm diameter microdroplet, an almost uniform distribution of γ-FeOOH was observed throughout the whole space of the microdroplet after about 3 min (Figure S15C). Undoubtedly, the unique air-water interface properties (e.g., species enrichment and pH alternation) of microdroplets are favorable to the faster interfacial photoreaction. Although the light irradiation near the interfacial region of the microdroplet is not as efficient as that in the microdroplet interior, this adverse effect on interface photoreaction is not significant, as indicated by the faster γ-FeOOH formation near the interfacial region. Besides, for small microdroplets, the O_2 transfer and availability in whole space is highly efficient as shown in Figure 4C. Thus, the strengthened light illumination in the microdroplet interior is also favorable to the photoreaction acceleration.

Evaporation is inevitable during microdroplet photoreaction, although this is greatly suppressed in our system through low-temperature and high-humidity control. However, the volatilization of the organic molecule is not the reason behind the improved photodegradation. As shown in the N_2 atmosphere experiment (Figure S7), hardly any decrease of MO concentration is observed, in consistency with that expected from a vapor pressure. An increase in the concentration of reactants due to water evaporation is ruled out as a potential reason. Even the reactant concentration was deliberately increased 5-fold, the MO photodegradation rate was increased only 3.81 times (Figure S12B). In addition, there was hardly any organic removal under 785 nm Raman laser radiation and in the absence of Fe(III)-oxalate chelates and g-C_3N_4 (Figures S17 and S18). Moreover, air purge and magnetic stirring in bulk solution to improve O_2 supply and reagent transfer were also studied and compared. As shown in Figure S19, the MO photodegradation rate is correspondingly increased by only 2.41 and 2.94 times in bulk phase. All these results confirmed the superiority of microdroplets.

Scale-up tests

Finally, we demonstrated the large-scale applicability of microdroplet photochemistry and photocatalysis; the methods used are well known.[55,56] An electric nebulizer was used to generate a large number of microdroplets ($\Phi < 50$ μm) from the Fe(III)-oxalate solution. The MO photodegradation rate (6.31 mg L^{-1} min^{-1}; Figure 6A) was found to be approximately 15.1 times higher than that of bulk phase (0.42 mg L^{-1} min^{-1}). The enhancement was lower than that of individual
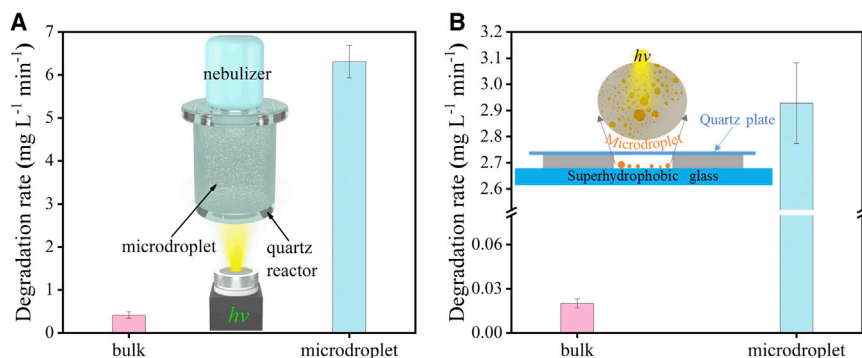
Figure 6. Scale-up tests of microdroplet photoreaction
(A) MO photochemical degradation by Fe(III)-oxalate photochemistry.
(B) Photocatalytic MO degradation by g-C$_3$N$_4$ photocatalysis. The error bars represent standard deviation of at least three repeats. The insets are the corresponding schematic setup for microdroplets generation and photoreaction.

microdroplet, which might be because (1) the suspended microdroplets significantly inhibited light penetration due to scattering effect (Figure S20), (2) some microdroplets adhered to the wall of the quartz reactor, and (3) the average reaction time for microdroplet is shorter than that for bulk phase owing to the consecutive spray. The scale up of g-C$_3$N$_4$ photocatalytic MO degradation in microdroplets (averaged diameter, 270 μm; Figure S21) was conducted in a custom-designed environmental control chamber. The MO photodegradation rate (2.92 mg L^{-1} min^{-1}; Figure 6B) is about 145-fold higher than that of the bulk-phase reaction (0.02 mg L^{-1} min^{-1}). Although presently the scale-up tests are at the proof-of-principle stage, with dimensions of 30 × 20 × 200 mm, our experimental results clearly stimulate interest in additional studies on microdroplet photochemistry and photocatalysis.

In summary, significantly accelerated (up to two orders of magnitude) photochemical and photocatalytic reactions in microdroplets were demonstrated via micro-Raman spectroscopy. SRS chemical imaging provided experimental evidence for the uniqueness of reactant concentration enrichment near the air-water interface and pH alternation in microdroplets. In combination with the dramatically improved O$_2$ transfer and availability, the organic photodegradation in microdroplets was remarkably increased by decreasing the microdroplets diameter. The scalability of the microdroplet photoreactions were also demonstrated. Microdroplets provide a very efficient pathway for accelerating chemical reactions limited by gas diffusion in liquid, benefiting photocatalysis and photochemical conversion for environmental, energy, and green synthesis. Furthermore, because cloud and fog droplets and sea spray are almost in the range of micrometers, this study also shows important implications on atmospheric photochemistry.

EXPERIMENTAL PROCEDURES

Resource availability

Lead contact
Further information and requests for resources should be directed to the corresponding author, Liwu Zhang (zhanglw@fudan.edu.cn).

Materials availability
This study did not generate new unique reagents.

Data and code availability
All data are available from the lead contact upon reasonable request.

SUPPLEMENTAL INFORMATION

ACKNOWLEDGMENTS

AUTHOR CONTRIBUTIONS

Conceptualization, L.Z. and K.L.; methodology, K.L., K.G., L.O., and M.J.; investigation, K.L., K.G., J.A., Y.L., X.C., and G.S.; writing – original draft, K.L.; writing – review & editing, L.Z., L.O., and V.K.V.; funding acquisition, L.Z., V.K.V., and J.H.; software, J.L., G.X., X.R., H.C., and K.G.; supervision, L.Z.

DECLARATION OF INTERESTS

The authors declare no competing interests.

REFERENCES

1. Colmenares, J.C., and Luque, R. (2014). Heterogeneous photocatalytic nanomaterials: prospects and challenges in selective transformations of biomass-derived compounds. Chem. Soc. Rev. *43*, 765–778. https://doi.org/10.1039/c3cs60262a.

2. Takata, T., Jiang, J., Sakata, Y., Nakabayashi, M., Shibata, N., Nandal, V., Seki, K., Hisatomi, T., and Domen, K. (2020). Photocatalytic water splitting with a quantum efficiency of almost unity. Nature *581*, 411–414. https://doi.org/10.1038/s41586-020-2278-9.

3. Sheng, X., Liu, Z., Zeng, R., Chen, L., Feng, X., and Jiang, L. (2017). Enhanced photocatalytic reaction at air–liquid–solid joint interfaces. J. Am. Chem. Soc. *139*, 12402–12405. https://doi.org/10.1021/jacs.7b07187.

4. Schultz, T., Lungwitz, D., Longhi, E., Barlow, S., Marder, S.R., and Koch, N. (2021). The interlayer method: a universal tool for energy level alignment tuning at inorganic/organic semiconductor heterojunctions. Adv. Funct. Mater. *31*, 2010174. https://doi.org/10.1002/adfm.202010174.

5. Hayyan, M., Hashim, M.A., and AlNashef, I.M. (2016). Superoxide ion: generation and chemical implications. Chem. Rev. *116*, 3029–3085. https://doi.org/10.1021/acs.chemrev.5b00407.

6. Xu, X., Yang, N., Wang, P., Wang, S., Xiang, Y., Zhang, X., Ding, X., and Chen, H. (2019). Highly intensified molecular oxygen activation on Bi@Bi$_2$MoO$_6$ via a metallic Bi-coordinated facet-dependent effect. ACS Appl. Mater. Inter. *12*, 1867–1876. https://doi.org/10.1021/acsami.9b17623.

7. Li, J., Chen, G., Zhu, Y., Liang, Z., Pei, A., Wu, C.L., Wang, H., Lee, H.R., Liu, K., Chu, S., and Cui, Y. (2018). Efficient electrocatalytic CO$_2$ reduction on a three-phase interface. Nat. Catal. *1*, 592–600. https://doi.org/10.1038/s41929-018-0108-3.

8. Roduner, E. (2006). Size matters: why nanomaterials are different. Chem. Soc. Rev. *35*, 583–592. https://doi.org/10.1039/B502142C.

9. Rao, C.N.R., and Cheetham, A.K. (2001). Science and technology of nanomaterials: current status and future prospects. J. Mater. Chem. *11*, 2887–2894. https://doi.org/10.1039/B105058N.

10. Bzdek, B.R., Reid, J.P., and Cotterell, M.I. (2020). Open questions on the physical properties of aerosols. Commun. Chem. *3*, 105. https://doi.org/10.1038/s42004-020-00342-9.

11. Hu, J., Wang, T., Zhang, W., Hao, H., Yu, Q., Gao, H., Zhang, N., Chen, Y., Xia, X., Chen, H., and Xu, J. (2021). Dissecting the flash chemistry of electrogenerated reactive intermediates by microdroplet fusion mass spectrometry. Angew. Chem. Int. Ed. *60*, 18494–18498. https://doi.org/10.1002/anie.202106945.

12. Banerjee, S., and Zare, R.N. (2015). Syntheses of isoquinoline and substituted quinolines in charged microdroplets. Angew. Chem. Int. Ed. *54*, 14795–14799. https://doi.org/10.1002/anie.201507805.

13. Müller, T., Badu-Tawiah, A., and Cooks, R.G. (2012). Accelerated carbon-carbon bond-forming reactions in preparative electrospray.

Angew. Chem. Int. Ed. *51*, 11832–11835. https://doi.org/10.1002/anie.201206632.

14. Badu-Tawiah, A.K., Campbell, D.I., and Cooks, R.G. (2012). Accelerated C–N bond formation in dropcast thin films on ambient surfaces. J. Am. Soc. Mass Spectrom. *23*, 1461–1468. https://doi.org/10.1007/s13361-012-0394-y.

15. Hung, H.-M., and Hoffmann, M.R. (2015). Oxidation of gas-phase SO_2 on the durfaces of acidic microdroplets: implications for sulfate and sulfate radical anion formation in the atmospheric liquid phase. Environ. Sci. Technol. *49*, 13768–13776. https://doi.org/10.1021/acs.est.5b01658.

16. Angle, K.J., Neal, E.E., and Grassian, V.H. (2021). Enhanced rates of transition-metal-ion-catalyzed oxidation of S(IV) in aqueous aerosols: insights into sulfate aerosol formation in the atmosphere. Environ. Sci. Technol. *55*, 10291–10299. https://doi.org/10.1021/acs.est.1c01932.

17. Liu, T., and Abbatt, J.P.D. (2021). Oxidation of sulfur dioxide by nitrogen dioxide accelerated at the interface of deliquesced aerosol particles. Nat. Chem. *13*, 1173–1177. https://doi.org/10.1038/s41557-021-00777-0.

18. Gu, A.Y., Musgrave, C., Goddard, W.A., Hoffmann, M.R., and Colussi, A.J. (2021). Role of ferryl ion intermediates in fast Fenton chemistry on aqueous microdroplets. Environ. Sci. Technol. *55*, 14370–14377. https://doi.org/10.1021/acs.est.1c01962.

19. Feng, L., Yin, X., Tan, S., Li, C., Gong, X., Fang, X., and Pan, Y. (2021). Ammonium bicarbonate significantly accelerates the microdroplet reactions of amines with carbon dioxide. Anal. Chem. *93*, 15775–15784. https://doi.org/10.1021/acs.analchem.1c03954.

20. Zhang, W., Cheng, H., and Liu, J. (2018). Accelerated two-phase oxidation in microdroplets assisted by light and heat without the use of phase-transfer catalysts. ACS Sustain. Chem. Eng. *6*, 8125–8129. https://doi.org/10.1021/acssuschemeng.8b01430.

21. Lee, J.K., Samanta, D., Nam, H.G., and Zare, R.N. (2019). Micrometer-sized water droplets induce spontaneous reduction. J. Am. Chem. Soc. *141*, 10585–10589. https://doi.org/10.1021/jacs.9b03227.

22. Lee, J.K., Samanta, D., Nam, H.G., and Zare, R.N. (2018). Spontaneous formation of gold nanostructures in aqueous microdroplets. Nat. Commun. *9*, 1562–1569. https://doi.org/10.1038/s41467-018-04023-z.

23. Lee, J.K., Walker, K.L., Han, H.S., Kang, J., Prinz, F.B., Waymouth, R.M., Nam, H.G., and Zare, R.N. (2019). Spontaneous generation of hydrogen peroxide from aqueous microdroplets. Proc. Natl. Acad. Sci. U S A *116*, 19294–19298. https://doi.org/10.1073/pnas.1911883116.

24. Wang, W., Qiao, L., He, J., Ju, Y., Yu, K., Kan, G., Guo, C., Zhang, H., and Jiang, J. (2021). Water microdroplets allow spontaneously abiotic production of peptides. J. Phys. Chem. Lett. *12*, 5774–5780. https://doi.org/10.1021/acs.jpclett.1c01083.

25. Wei, Z., Li, Y., Cooks, R.G., and Yan, X. (2020). Accelerated reaction kinetics in microdroplets: overview and recent developments. Annu. Rev. Phys. Chem. *71*, 31–51. https://doi.org/10.1146/annurev-physchem-121319-110654.

26. Xiong, H., Lee, J.K., Zare, R.N., and Min, W. (2020). Strong electric field observed at the interface of aqueous microdroplets. J. Phys. Chem. Lett. *11*, 7423–7428. https://doi.org/10.1021/acs.jpclett.0c02061.

27. Wei, H., Vejerano, E.P., Leng, W., Huang, Q., Willner, M.R., Marr, L.C., and Vikesland, P.J. (2018). Aerosol microdroplets exhibit a stable pH gradient. Proc. Natl. Acad. Sci. U S A *115*, 7272–7277. https://doi.org/10.1073/pnas.1720488115.

28. Rubio, D., Nebot, E., Casanueva, J.F., and Pulgarin, C. (2013). Comparative effect of simulated solar light, UV, UV/H_2O_2 and photo-Fenton treatment ($UV–Vis/H_2O_2/Fe^{2+,3+}$) in the Escherichia coli inactivation in artificial seawater. Water Res. *47*, 6367–6379. https://doi.org/10.1016/j.watres.2013.08.006.

29. Song, R., Chi, H., Ma, Q., Li, D., Wang, X., Gao, W., Wang, H., Wang, X., Li, Z., and Li, C. (2021). Highly efficient degradation of persistent pollutants with 3D nanocone TiO_2-based photoelectrocatalysis. J. Am. Chem. Soc. *143*, 13664–13674. https://doi.org/10.1021/jacs.1c05008.

30. Chen, S., Wan, Q., and Badu-Tawiah, A.K. (2016). Picomole-ccale real-time photoreaction screening: discovery of the visible-light-promoted dehydrogenation of tetrahydroquinolines under ambient conditions. Angew. Chem. Int. Ed. *55*, 9345–9349. https://doi.org/10.1002/anie.201603530.

31. Pang, H., Zhang, Q., Wang, H., Cai, D., Ma, Y., Li, L., Li, K., Lu, X., Chen, H., Yang, X., and Chen, J. (2018). Photochemical aging of guaiacol by Fe(III)–oxalate complexes in atmospheric aqueous phase. Environ. Sci. Technol. *53*, 127–136. https://doi.org/10.1021/acs.est.8b04507.

32. Yu, X., Sun, J., Li, G., Huang, Y., Li, Y., Xia, D., and Jiang, F. (2020). Integration of $\cdot SO_4^-$-based AOP mediated by reusable iron particles and a sulfidogenic process to degrade and detoxify Orange II. Water Res. *174*, 115622. https://doi.org/10.1016/j.watres.2020.115622.

33. Wang, T., Liu, Y., Deng, Y., Cheng, H., Yang, Y., Feng, Y., Zhang, L., Fu, H., and Chen, J. (2020). Photochemical oxidation of water-soluble organic carbon (WSOC) on mineral dust and enhanced organic ammonium formation. Environ. Sci. Technol. *54*, 15631–15642. https://doi.org/10.1021/acs.est.0c04616.

34. Duan, X., Sun, H., Shao, Z., and Wang, S. (2018). Nonradical reactions in environmental remediation processes: uncertainty and challenges. Appl. Catal. B Environ. *224*, 973–982. https://doi.org/10.1016/j.apcatb.2017.11.051.

35. Luo, B., Xu, D., Li, D., Wu, G., Wu, M., Shi, W., and Chen, M. (2015). Fabrication of a Ag/Bi_3TaO_7 plasmonic photocatalyst with enhanced photocatalytic activity for degradation of tetracycline. ACS Appl. Mater. Inter. *7*, 17061–17069. https://doi.org/10.1021/acsami.5b03535.

36. Zhou, H., Sheng, X., Xiao, J., Ding, Z., Wang, D., Zhang, X., Liu, J., Wu, R., Feng, X., and Jiang, L. (2020). Increasing the efficiency of photocatalytic reactions via surface microenvironment engineering. J. Am. Chem. Soc. *142*, 2738–2743. https://doi.org/10.1021/jacs.9b12247.

37. Song, Z., Xu, C., Sheng, X., Feng, X., and Jiang, L. (2018). Utilization of peroxide reduction reaction at air–liquid–solid joint interfaces for reliable sensing system construction. Adv. Mater. *30*, 1701473. https://doi.org/10.1002/adma.201701473.

38. Zhang, Q., Zhou, M., Ren, G., Li, Y., Li, Y., and Du, X. (2020). Highly efficient electrosynthesis of hydrogen peroxide on a superhydrophobic three-phase interface by natural air diffusion. Nat. Commun. *11*, 1731. https://doi.org/10.1038/s41467-020-15597-y.

39. Craig, R.L., Nandy, L., Axson, J.L., Dutcher, C.S., and Ault, A.P. (2017). Spectroscopic determination of aerosol pH from acid–base equilibria in inorganic, organic, and mixed systems. J. Phys. Chem. A *121*, 5690–5699. https://doi.org/10.1021/acs.jpca.7b05261.

40. Craig, R.L., Peterson, P.K., Nandy, L., Lei, Z., Hossain, M.A., Camarena, S., Dodson, R.A., Cook, R.D., Dutcher, C.S., and Ault, A.P. (2018). Direct determination of aerosol pH: size-resolved measurements of submicrometer and supermicrometer aqueous particles. Anal. Chem. *90*, 11232–11239. https://doi.org/10.1021/acs.analchem.8b00586.

41. Girod, M., Moyano, E., Campbell, D.I., and Cooks, R.G. (2011). Accelerated bimolecular reactions in microdroplets studied by desorption electrospray ionization mass spectrometry. Chem. Sci. *2*, 501–510. https://doi.org/10.1039/C0SC00416B.

42. Wang, Y., Zhao, J., Liu, H., Li, Y., Dong, W., and Wu, Y. (2021). Photooxidation of methacrolein in Fe(III)-Oxalate aqueous system and its atmospheric implication. Adv. Atmos. Sci. *38*, 1252–1263. https://doi.org/10.1007/s00376-021-0415-5.

43. Huang, K.-H., Wei, Z., and Cooks, R.G. (2021). Accelerated reactions of amines with carbon dioxide driven by superacid at the microdroplet interface. Chem. Sci. *12*, 2242–2250. https://doi.org/10.1039/D0SC05625A.

44. Sagar, D.M., Bain, C.D., and Verlet, J.R.R. (2010). Hydrated electrons at the water/air interface. J. Am. Chem. Soc. *132*, 6917–6919. https://doi.org/10.1021/ja101176r.

45. Anglada, J.M., Martins-Costa, M.T.C., Francisco, J.S., and Ruiz-López, M.F. (2020). Photoinduced oxidation reactions at the air–water interface. J. Am. Chem. Soc. *142*, 16140–16155. https://doi.org/10.1021/jacs.0c06858.

46. Aarnoutse, P.J., and Westerhuis, J.A. (2005). Quantitative raman reaction monitoring using the solvent as internal standard. Anal. Chem. *77*, 1228–1236. https://doi.org/10.1021/ac0401523.

47. Enami, S., Fujii, T., Sakamoto, Y., Hama, T., and Kajii, Y. (2016). Carboxylate ion availability at the air–water interface. J. Phys. Chem. A *120*, 9224–9234. https://doi.org/10.1021/acs.jpca.6b08868.

48. Xiong, H., Lee, J.K., Zare, R.N., and Min, W. (2020). Strong concentration enhancement of

molecules at the interface of aqueous microdroplets. J. Chem. Phys. B *124*, 9938–9944. https://doi.org/10.1021/acs.jpcb.0c07718.

49. Yan, X., Bain, R.M., and Cooks, R.G. (2016). Organic reactions in microdroplets: reaction acceleration revealed by mass spectrometry. Angew. Chem. Int. Ed. *55*, 12960–12972. https://doi.org/10.1002/anie.201602270.

50. Lin, L., Husek, J., Biswas, S., Baumler, S.M., Adel, T., Ng, K.C., Baker, L.R., and Allen, H.C. (2019). Iron(III) speciation observed at aqueous and glycerol surfaces: vibrational sum frequency and X-ray. J. Am. Chem. Soc. *141*, 13525–13535. https://doi.org/10.1021/jacs.9b05231.

51. Martins-Costa, M.T.C., Anglada, J.M., Francisco, J.S., and Ruiz-Lopez, M.F. (2012).

Reactivity of atmospherically relevant small radicals at the air–water interface. Angew. Chem. Int. Ed. *51*, 5413–5417. https://doi.org/10.1002/anie.201200656.

52. Chamberlayne, C.F., and Zare, R.N. (2020). Simple model for the electric field and spatial distribution of ions in a microdroplet. J. Chem. Phys. *152*, 184702. https://doi.org/10.1063/5.0006550.

53. de Faria, D.L.A., Venâncio Silva, S., and de Oliveira, M.T. (1997). Raman microspectroscopy of some iron oxides and oxyhydroxides. J. Raman Spectrosc. *28*, 873–878. https://doi.org/10.1002/(SICI)1097-4555(199711)28:113.0.CO;2-B.

54. Nguyen, T., and Fátima Montemor, M. (2018). γ-FeOOH and amorphous Ni–Mn hydroxide

on carbon nanofoam paper electrodes for hybrid supercapacitors. J. Mater. Chem. A 6, 2612–2624. https://doi.org/10.1039/C7TA05582J.

55. Yan, X., Lai, Y.-H., and Zare, R.N. (2018). Preparative microdroplet synthesis of carboxylic acids from aerobic oxidation of aldehydes. Chem. Sci. 9, 5207–5211. https://doi.org/10.1039/C8SC01580E.

56. Gong, C., Li, D., Li, X., Zhang, D., Xing, D., Zhao, L., Yuan, X., and Zhang, X. (2022). Spontaneous reduction-induced degradation of viologen compounds in water microdroplets and its inhibition by host–guest complexation. J. Am. Chem. Soc. *144*, 3510–3516. https://doi.org/10.1021/jacs.1c12028.